Cell Reports

Report

Longitudinal Alzheimer's Degeneration Reflects the Spatial Topography of Cholinergic Basal Forebrain Projections

Graphical Abstract

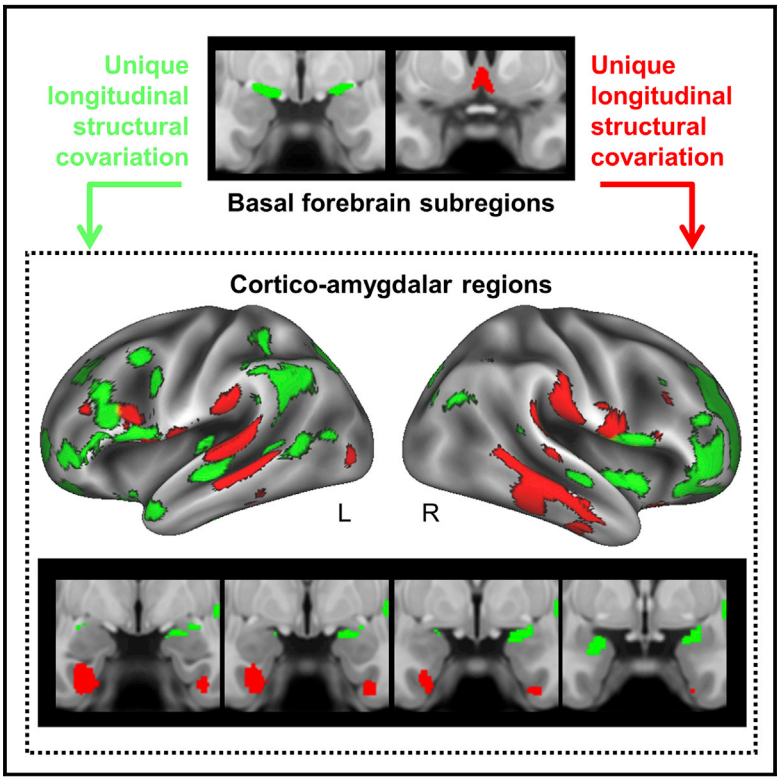

Authors

Taylor W. Schmitz, Marieke Mur, Meghmik Aghourian, Marc-Andre Bedard, R. Nathan Spreng, for the Alzheimer's Disease Neuroimaging Initiative

Correspondence

taylor.schmitz@gmail.com

In Brief

Among older adults in prodromal stages of Alzheimer's disease, Schmitz et al. show that longitudinal degeneration within sub-regions of the basal forebrain covaries with cortico-amygdalar topographies of both structural degeneration and cholinergic denervation. The findings support the view that loss of cortico-amygdalar cholinergic input is a pivotal event in AD progression.

Highlights

- The basal forebrain degenerates substantially in early Alzheimer's disease (AD)
- Longitudinal gray matter loss in the basal forebrain, cortex, and amygdalae covaries
- This covariation reflects the organization of the basal forebrain cholinergic projections
- This covariation also reflects [^{18}F] FEOBV PET indices of cholinergic denervation

Schmitz et al., 2018, Cell Reports *24*, 38–46
July 3, 2018
https://doi.org/10.1016/j.celrep.2018.06.001

CellPress

OPEN ACCESS
CellPress

Cell Reports
Report

Longitudinal Alzheimer's Degeneration Reflects the Spatial Topography of Cholinergic Basal Forebrain Projections

Taylor W. Schmitz,[1,7,*] Marieke Mur,[2] Meghmik Aghourian,[3,4,5] Marc-Andre Bedard,[3,4,5] and R. Nathan Spreng,[1,6] for the Alzheimer's Disease Neuroimaging Initiative

[1]Department of Neurology and Neurosurgery, Montreal Neurological Institute, McGill University, Montreal, QC, Canada
[2]Medical Research Council Cognition and Brain Sciences Unit, University of Cambridge, Cambridge, UK
[3]Cognitive Pharmacology Research Unit, Université du Québec à Montréal (UQAM), Montreal, QC, Canada
[4]McConnell Brain Imaging Centre, Montreal Neurological Institute, Montreal, QC, Canada
[5]McGill Centre for Studies in Aging, Douglas Mental Health University Institute, Verdun, QC, Canada
[6]Department of Human Development, Human Neuroscience Institute, Cornell University, Ithaca, NY, USA
[7]Lead Contact
*Correspondence: taylor.schmitz@gmail.com
https://doi.org/10.1016/j.celrep.2018.06.001

SUMMARY

The cholinergic neurons of the basal forebrain (BF) provide virtually all of the brain's cortical and amygdalar cholinergic input. They are particularly vulnerable to neuropathology in early Alzheimer's disease (AD) and may trigger the emergence of neuropathology in their cortico-amygdalar projection system through cholinergic denervation and *trans*-synaptic spreading of misfolded proteins. We examined whether longitudinal degeneration within the BF can explain longitudinal cortico-amygdalar degeneration in older human adults with abnormal cerebrospinal fluid biomarkers of AD neuropathology. We focused on two BF subregions, which are known to innervate cortico-amygdalar regions via two distinct macroscopic cholinergic projections. To further assess whether structural degeneration of these regions in AD reflects cholinergic denervation, we used the [^{18}F] FEOBV radiotracer, which binds to cortico-amygdalar cholinergic terminals. We found that the two BF subregions explain spatially distinct patterns of cortico-amygdalar degeneration, which closely reflect their cholinergic projections, and overlap with [^{18}F] FEOBV indices of cholinergic denervation.

INTRODUCTION

The emergence of Alzheimer's disease (AD) neuropathologies, such as misfolded β-amyloid (Aβ) and Tau proteins, progresses in stages across anatomically and functionally connected regions of the brain, with certain brain regions affected before others (Braak and Braak, 1991; Braak and Del Tredici, 2015; Raj et al., 2012, 2015; Seeley et al., 2009). Why certain brain regions appear more vulnerable to AD pathology than others has long remained a mystery. However, recent functional genomics research, using brain tissue in both human AD and non-human animal models of AD, has started to elucidate structural and functional cell characteristics that predict selective neuronal vulnerability to AD pathology. Vulnerable neurons typically have large axonal projections that extend relatively long distances, from one region of the brain to another. As a result, they require high metabolic expenditure to maintain trophic support—transporting materials over long distances and maintaining enormous cytoskeletal surface areas. These morphological properties increase vulnerability to oxidative stress and neuroinflammation, perturbed energy homeostasis, and accumulation of misfolded proteins (Lewis et al., 2010; Mattson and Magnus, 2006; Wang et al., 2010).

The magnocellular cholinergic neurons in the basal forebrain (BF) are known to have very large projections, targeting distal areas of the cortical mantle and amygdalae via multiple routes such as the cingulum bundle (Bloem et al., 2014; Chandler et al., 2013; Hecker and Mesulam, 1994; Kondo and Zaborszky, 2016; Mesulam et al., 1983a, 1986; Zaborszky et al., 2015). Precise estimates of their size have been difficult to obtain due to the complexity of their axonal branching. Recently, however, the complete morphology of individual cholinergic neurons was visualized in mice using a novel cell labeling technique (Wu et al., 2014). Extrapolating from their results, the authors estimated that cholinergic projections in humans approach ~100 m in length for a single cell when accounting for all axonal branches. As a result of their exceptional size, cholinergic neurons are therefore likely to exhibit selective neuronal vulnerability (SNV) to AD pathology.

Consistent with the SNV model, post-mortem histological evidence suggests that the cholinergic BF neurons accumulate both intraneuronal Tau, and, interestingly, intraneuronal Aβ as early as the third decade of life, with profound accumulation observed 1 year after transition to mild cognitive impairment (MCI) (Arendt et al., 2015; Baker-Nigh et al., 2015; Braak and Braak, 1991; Braak and Del Tredici, 2015; Geula et al., 2008; Mesulam et al., 2004; Mesulam, 2013; Schliebs and Arendt, 2006, 2011). *In vivo* neuroimaging data have demonstrated that

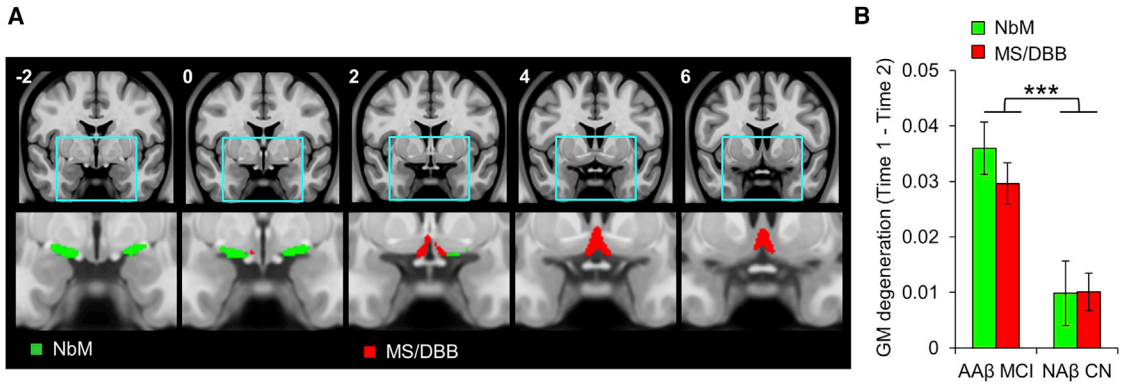

Figure 1. Basal Forebrain Regions of Interest and Longitudinal Degeneration in Early AD

(A) Regions of interest (ROIs) were defined from stereotaxic probabilistic maps of the human basal forebrain (Zaborszky et al., 2008). The nucleus basalis of Meynert (NbM) is displayed in green. The medial septal nucleus and diagonal band of Broca (MS/DBB) are displayed in red. The ROIs are projected on coronal slices in standard atlas space (MNI y coordinates are inset).

(B) Longitudinal degeneration (y axis) of both NbM and MS/DBB was elevated among individuals with abnormal cerebrospinal levels of the amyloid-β biomarker and mild cognitive impairment (AAβ MCI) relative to age-matched controls with normal Aβ and cognitive function (NAβ CN). y axis units are averaged gray matter volume within each ROI ± SEM.

cognitively normal (CN) older adults expressing abnormal cerebrospinal fluid (CSF) biomarkers of Aβ accumulation, i.e., individuals in preclinical stages of AD, exhibit greater longitudinal degeneration in the BF compared to CN adults with normal CSF Aβ (Schmitz and Spreng, 2016). Furthermore, total gray matter volume in the BF at baseline was found to predict subsequent longitudinal degeneration in the entorhinal cortex—a major target of cholinergic innervation (Kondo and Zaborszky, 2016)—and memory impairment. Competing models using baseline volume in entorhinal cortex to predict longitudinal degeneration in BF were not supported (Schmitz and Spreng, 2016). These findings suggest a potential interdependence between degeneration in the BF and the cholinoreceptive cortical targets of its projection system.

Research in non-human animals strongly supports this possibility. In mice bred to express a genetic knockout or knockdown of the vesicular acetylcholine transporter (VAChT, SLC18A3), a protein required for acetylcholine (ACh) release from cholinergic BF neurons (de Castro et al., 2009; Prado et al., 2013), long-term cholinergic deficiency leads to abnormal accumulation of Aβ and Tau in cholinoreceptive cortical neurons (Kolisnyk et al., 2016, 2017). These data suggest a role for cholinergic signaling in maintaining normal cell metabolism, including native biological functions related to the amyloid precursor and Tau proteins. In parallel to cholinergic denervation, intact but diseased cholinergic inputs might facilitate yet another mechanism of "seeding" the cortex with AD pathology, specifically through the *trans*-synaptic spread of misfolded Tau fragments (Clavaguera et al., 2009; de Calignon et al., 2012; Khan et al., 2014).

If the emergence of AD pathology in the cortex is caused by the loss of cortical cholinergic input or *trans*-synaptic spreading of Tau from cholinergic neurons, then the spatial topography of cortico-amygdalar degeneration should reflect the cholinergic projection system. The cholinergic BF projections exhibit topographical organization at multiple spatial scales (Ballinger et al., 2016; Bloem et al., 2014; Kondo and Zaborszky, 2016; Mesulam and Geula, 1988; Mesulam et al., 1983b, 1986; Zaborszky et al., 2015). To accommodate the spatial scale of high-resolution structural magnetic resonance imaging (MRI) data employed in the present study, we chose a topography that divides the BF into two segregated macroscopic projections (Zaborszky et al., 2008), the medial septal nucleus and diagonal band of Broca (MS/DBB) projection targeting medial temporal lobe, and the nucleus basalis of Meynert (NbM) projection targeting frontoparietal cortices and the amygdalae (Figures 1A and S1; Experimental Procedures). Structural properties such as gray matter volume are known to selectively co-vary between brain regions that are functionally and anatomically connected (Alexander-Bloch et al., 2013; Bassett et al., 2008; Cantero et al., 2017; Chen et al., 2008; Dupre and Spreng, 2017; He et al., 2007; Kilimann et al., 2017; Schmitz and Spreng, 2016; Spreng and Turner, 2013), enabling us to test the covariance in longitudinal structural degeneration between the BF and distinct targets of its cholinergic projections in the cortex and amygdalae.

Longitudinal voxel-based morphometry was used to measure changes in BF and cortico-amygdalar gray matter (GM) volume over a 2-year interval in older adults with mild cognitive impairment (MCI) and the CSF-Aβ biomarker of central AD pathology (Shaw et al., 2009). These data were acquired from the Alzheimer's Disease Neuroimaging Initiative (Mueller et al., 2005). Voxel-based morphometry was used to derive longitudinal indices of GM degeneration within the BF sub-regions (Grothe et al., 2018). We then performed a "seed-to-searchlight" analysis to determine whether the BF MS/DBB and NbM sub-regions (the "seeds") exhibit unique patterns of covariation with regions of cortex (the "searchlights"). We then compared these maps against a direct *in vivo* assay of cortical cholinergic denervation using the positron emission tomography (PET) radiotracer [^{18}F] FEOBV, which exhibits high binding sensitivity and specificity to VAChT (Aghourian et al., 2017). We show that in AD, topographies of longitudinal cortical degeneration covary with

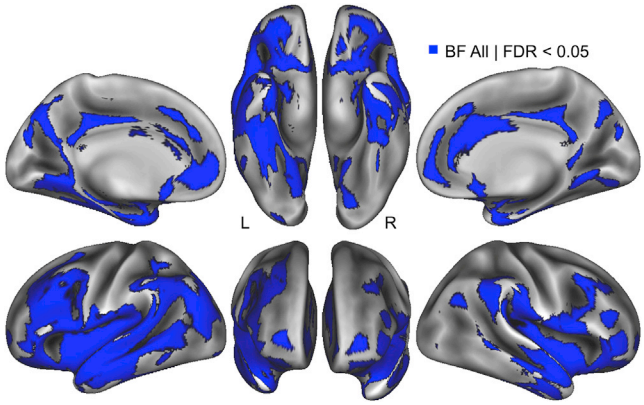

Figure 2. Spatial Topography of Covariance between BF and Cortical Degeneration

Seed-to-searchlight analysis tested whether BF degeneration (averaged over NbM and MS/DBB sub-regions) covaried with cortical degeneration within 6 mm radius spherical "searchlight" ROIs in the AAβ MCI group, controlling for age, sex, education, total intracranial volume, and longitudinal change in whole brain volume. Significant searchlights (blue overlay) were determined using a false discovery rate (FDR)-corrected $p < 0.05$. Results are projected on an inflated cortical surface in MNI atlas space.

longitudinal degeneration of the NbM and MS/DBB and closely reflect the known anatomical organization of the cortical cholinergic projection system, as well as the functional topographies of cortical cholinergic denervation assayed by [^{18}F] FEOBV PET.

RESULTS

The BF Exhibits Severe Longitudinal Degeneration in Early AD

To ensure the presence of AD pathology in our sample of older adults, independent of longitudinal structural MRI, we used the cerebrospinal fluid amyloid-β biomarker (CSF $A\beta_{1-42}$). Prior analyses of the ADNI core datasets (Shaw et al., 2009) have provided a cutpoint for CSF $A\beta_{1-42}$ concentration at which diagnostic sensitivity and specificity to AD is maximal (192 pg mL^{-1}), yielding correct detection of 96.4% (<192 pg mL^{-1}) and correct rejection of 95.2% (>192 pg mL^{-1}) (Experimental Procedures). Only individuals with abnormal CSF $A\beta_{1-42}$ values (AAβ) falling below this cutpoint were included. Second, in order to ensure our sample was at a stage of AD characterized by longitudinal degeneration in amygdalar, allocortical, and neocortical areas (Grothe et al., 2013; Schmitz and Spreng, 2016), we further filtered individuals according to their neuropsychological status. Only individuals with a diagnosis of MCI based on the ADNI neuropsychological test battery were included. We included both MCI individuals who remained stable and converted to AD in the 2-year study interval. After triangulating AD pathology from CSF biomarker and neuropsychological measures, our final sample size of AAβ MCI adults was n = 80 (mean ± SD; CSF $A\beta_{1-42}$ concentration = 136.45 ± 25.31, range = 81–190). See Table S1 for demographic and neuropsychological information, as well as CSF total Tau and phosphorylated Tau indices. See Table S2 for individual ADNI research identifier numbers, sMRI image identifier numbers, and Aβ subgroup designation. Individuals presenting MCI neuropsychological status but normal CSF Aβ levels were excluded from all forthcoming analyses, as their cognitive symptoms are likely to be caused by non-AD pathology, for example, vascular dementia and hippocampal sclerosis. See Table S3 for excluded MCI participants.

We next confirmed that the AAβ MCI group exhibited abnormal longitudinal degeneration in the BF subregional ROIs: NbM and MS/DBB. To do so, we compared longitudinal GM changes (time 1 – time 2) in the AAβ MCI group against a control group of age-matched older adults with both normal CSF $A\beta_{1-42}$ values (NAβ) and normal neuropsychological status (NAβ CN: n = 52, mean ± SD; CSF $A\beta_{1-42}$ concentration = 242.46 ± 25.55, range = 196–300). These groups also differed significantly in their CSF concentrations of total Tau and phosphorylated Tau (Tables S1 and S2). A 2 (group) × 2 (BF ROI) repeated-measures ANOVA revealed a significant main effect of group ($F_{1,130} = 16.4$, $p < 0.001$), driven by significant between group differences in both BF subregions (NbM: $t_{130} = 3.5$, $p < 0.001$; MS/DBB: $t_{130} = 3.9$, $p < 0.001$) (Figure 1B). We did not observe a main effect of ROI ($F < 1$), or a group by ROI interaction ($F = 1$). Consistent with existing work on longitudinal structural degeneration of the BF in MCI (Grothe et al., 2013; Schmitz and Spreng, 2016), our initial findings indicate that the presence of AD pathology yielded large increases in the magnitude of degeneration in both BF nuclei over a 2-year interval compared to normally aging older adults.

Covariation of Longitudinal Degeneration between the BF and Cortico-Amygdalar Regions

Having confirmed abnormal BF degeneration in our MCI sample, we next conducted a regression-based seed-to-searchlight analysis using the entire BF (NbM and MS/DBB combined) as the seed region. Searchlight analyses test a statistical model in small spherical ROIs ("searchlights") centered on every voxel, as opposed to the individual voxels themselves (Kriegeskorte et al., 2006). At each searchlight, a multiple linear regression model was performed with mean longitudinal degeneration (time 1 – time 2) within the BF as the predictor, and nuisance covariates for age, sex, education, total intracranial volume, and longitudinal change in whole brain volume. The dependent variable was mean degeneration (time 1 – time 2) within the cortical searchlight. A significant searchlight indicates a covariation in longitudinal degeneration between the BF and the local neighborhood of voxels within the searchlight region.

Across AAβ MCI individuals, we found that larger magnitudes of longitudinal BF degeneration covaried with larger magnitudes of cortical degeneration in the frontal, temporal, and parietal cortices. The data were corrected for multiple comparisons using a false discovery (FDR) rate $p < 0.05$ (Figure 2). Spatial foci within these cortical areas are in close agreement with prior work showing preferential vulnerability to AD pathology in anterior medial temporal cortex, cingulate cortex, and lateral frontoparietal cortices (Buckner et al., 2005). We also observed significant covariation bilaterally in the amygdalae.

We conducted a second seed-to-searchlight analysis in the NAβ CN group, using the same model specifications as in the AAβ MCI group. However, this model failed to detect suprathreshold cortical degeneration after correction for multiple

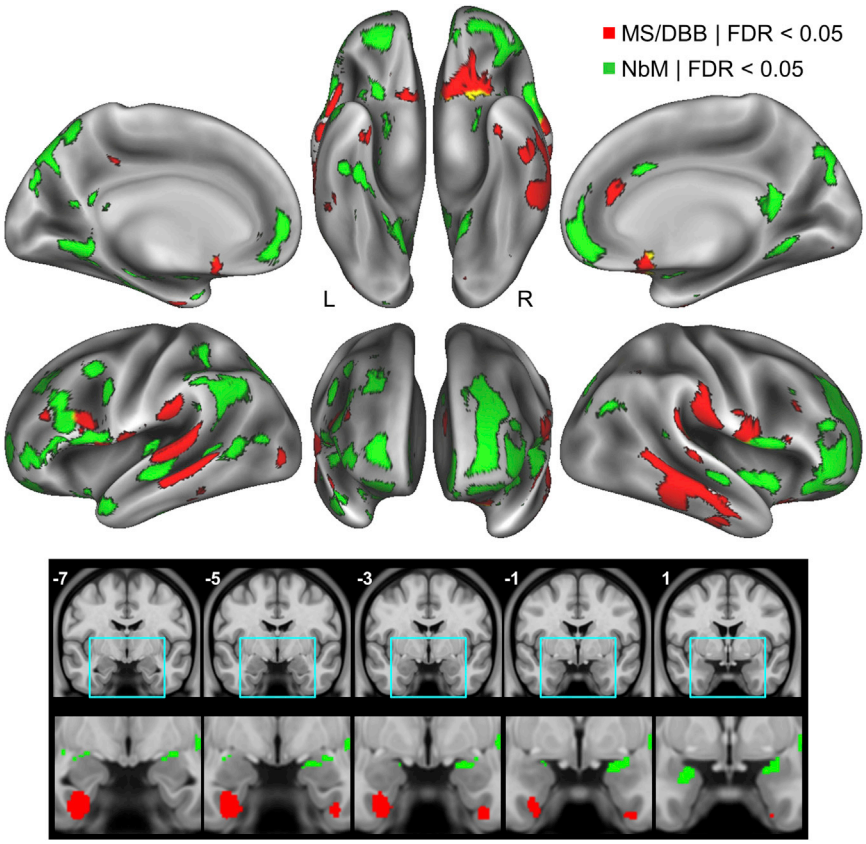

Figure 3. Degeneration within BF NbM and MS/DBB Nuclei Covaries with Distinct Spatial Topographies of Degeneration in Their Cortical Targets

Seed-to-searchlight analysis tested whether the NbM or MS/DBB BF subregions selectively covaried with cortical degeneration in the AAβ MCI group, controlling for degeneration in the opposing BF subregion (MS/DBB and NbM, respectively). The NbM selectively covaried with degeneration (green overlays) in distributed areas of frontal, parietal, and occipital cortex (top), as well as in the amygdalae (bottom). The MS/DBB selectively covaried with degeneration (red overlays) in more circumscribed areas of temporal cortex including the middle temporal gyrus (cortical surfaces), and the entorhinal cortices (bottom). Additional areas included the temporo-parietal and left inferior frontal cortices. Significant searchlights were determined using a FDR-corrected $p < 0.05$. Top: results are projected on an inflated cortical surface in MNI atlas space. Bottom: results are displayed on coronal slices in MNI atlas space (y coordinates are inset).

comparisons. Hence, these patterns do not appear to reflect normal age-related patterns of covariance between BF and cortical degeneration.

Cortico-Amygdalar Covariation with BF Subregions Reflects the Cholinergic BF Projections

Many of the spatial foci identified by this initial analysis are also known to be strongly innervated by the ascending cholinergic projections, including the entorhinal cortex, hippocampus, amygdalae, and medial prefrontal cortex (Bloem et al., 2014; Chandler et al., 2013; Hecker and Mesulam, 1994; Kondo and Zaborszky, 2016; Mesulam et al., 1986, 1983a; Zaborszky et al., 2015). However, the observed spatial topography may merely reflect coincidental degeneration of the BF, cortex, and amygdalae; AAβ MCI individuals with larger magnitudes of BF degeneration may tend to exhibit larger magnitudes of cortico-amygdalar degeneration due to parallel independent events. If this were the case, we would not expect degeneration within subregions of the BF to exhibit distinct patterns of covariation with degeneration in the cortex and amygdalae. Alternatively, if pathological events within the cholinergic BF subregions and their cortico-amygdalar targets are linked, longitudinal degeneration in NbM and MS/DBB should exhibit a pattern of cortico-amygdalar interdependence reflecting the distinct topography of their projections.

To adjudicate these competing alternatives, we conducted two modified seed-to-searchlight analyses on each BF subregion—NbM and MS/DBB—that are known to form segregated macroscopic projections to distinct areas of cortex and amygdalae. Each analysis examined whether mean longitudinal degeneration (time 1 – time 2) within either the NbM or MS/DBB ROI selectively covaried with mean degeneration within the cortical searchlights, while controlling for degeneration in the opposing subregion. As before, additional covariates included age, sex, education, total intracranial volume, and longitudinal change in whole brain volume.

Across AAβ MCI individuals, we observed that NbM and MS/DBB selectively covaried with distinct topographies of cortical degeneration that closely align with the segregated organization of their cholinergic projections (Figure 3). Higher magnitudes of NbM degeneration selectively covaried with higher magnitudes of degeneration in a more distributed topography reflecting its widespread cholinergic innervations of the frontal, parietal, and occipital cortices (Bloem et al., 2014; Mesulam and Geula, 1988; Mesulam et al., 1986, 1983a). The NbM also selectively covaried with higher focal degeneration in the amygdalae, an area which is densely innervated by its cholinergic projections (Hecker and Mesulam, 1994).

By contrast, the MS/DBB selectively covaried with higher magnitudes of degeneration in a more circumscribed topography. Degeneration within the temporal lobe, including the entorhinal cortex and extending laterally into the middle temporal gyri, are areas known to receive cholinergic innervations from the medial septal nucleus (MS) and vertical band of the DBB (Kondo and Zaborszky, 2016). Areas of MS/DBB covariation outside of the temporal cortex included the olfactory cortex, an area known to receive cholinergic projections from the horizontal band of the DBB (Mesulam et al., 1983a, 1986). Our longitudinal findings are consistent with cross-sectional studies

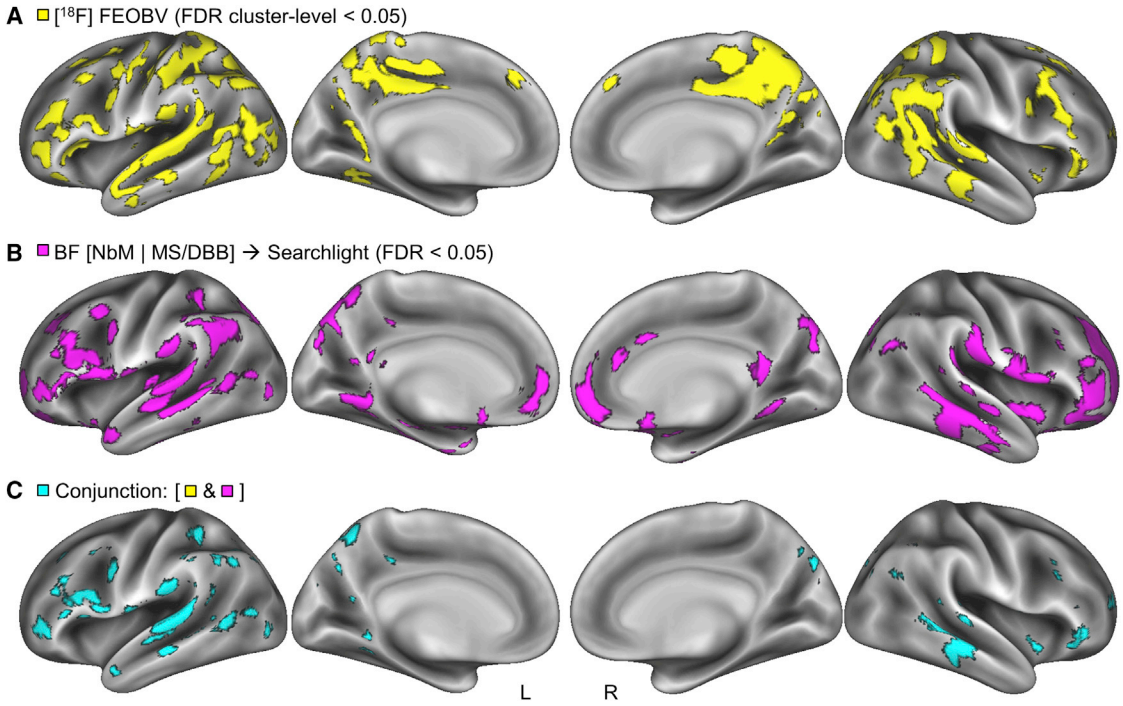

Figure 4. Spatial Convergence across Multimodal Indices of Cortical Cholinergic Degeneration

(A) A map of cortical cholinergic degeneration assayed by between group comparison of [^{18}F] FEOBV binding in cognitively normal versus AD adults (primary cluster forming threshold p uncorrected <0.001, secondary FDR cluster level threshold <0.05).

(B) A composite of the seed-to-searchlight maps for each BF subregion (Figure 3) was generated using a logical OR operation.

(C) A conjunction analysis (logical AND) was then applied to the FDR-corrected maps in (A) and (B). Results are projected on an inflated cortical surface in MNI atlas space.

demonstrating stronger inter-regional covariation of MS/DBB with hippocampal and amygdalar gray matter, and NbM with cingulate gray matter, in MCI compared to CN older adults (Cantero et al., 2017; Kilimann et al., 2017).

The subregional NbM and MS/DBB searchlight topographies were more spatially restricted than the searchlight topography observed in the initial analysis (both NbM and MS/DBB combined; Figure 2), especially in the cortical midline, indicating that the NbM and MS/DBB share common variance in these searchlight locations.

Convergent Structural and Functional Topographies of Cholinergic Degeneration

Our seed-to-searchlight structural degeneration maps suggest an interdependence between AD pathology within the BF projection system and its cortico-amygdalar targets. However, by itself, sMRI cannot determine whether the observed structural interdependencies (Figure 3) are specific to cortical cholinergic innervations. We therefore adopted a multimodal imaging strategy using the [^{18}F] FEOBV PET radiotracer, which exhibits a very high binding affinity and an excellent specificity for the vesicular acetylcholine transporter (VAChT), a glycoprotein found on the membrane of synaptic vesicles of cholinergic neurons (Aghourian et al., 2017; Cyr et al., 2014; Parent et al., 2012) (Figure S2; Table S4; Supplemental Experimental Procedures). The [^{18}F] FEOBV tracer provides an estimate of presynaptic neuronal integrity and is thought to remain unaffected by the post-synaptic activity of enzymes such as acetylcholinesterase (ACHE), although this has yet to be demonstrated *in vivo*. Cortical cholinergic denervation, whether induced experimentally via selective lesions of the BF nuclei in rats (Cyr et al., 2014; Parent et al., 2012), or due to AD pathology in humans (Aghourian et al., 2017), both alter regionally specific patterns of [^{18}F] FEOBV binding.

We first compared cognitively normal (n = 6) and AD (n = 6) older adults with indices of [^{18}F] FEOBV PET, collected as part of a prior study (Aghourian et al., 2017), to identify areas of significant cholinergic denervation. A two-sample t test controlling for age (Table S4; Experimental Procedures) revealed lower [^{18}F] FEOBV binding in the AD group spanning lateral fronto-parietal and temporal cortical areas. Due to the smaller sample sizes, we first imposed a cluster-forming threshold with an uncorrected $p < 0.001$, followed a cluster-level FDR-corrected $p < 0.05$ (Woo et al., 2014) (Figure 4A). We note that no differences were observed in the thalamus, medial temporal lobe, or amygdalar areas at the FDR-corrected threshold.

We next examined the precise areas of spatial convergence between the [^{18}F] FEOBV assay of cholinergic denervation (Figure 4A) and our seed-to-searchlight assay of BF-dependent structural degeneration (Figure 4B). To do so, a logical AND operation was performed on the FDR-corrected maps from each imaging modality (Nichols et al., 2005). The resulting

conjunction revealed tight correspondence in virtually all cortical areas of the left hemisphere. The right hemisphere exhibited lower spatial overlap, due in part to weaker effect sizes of clusters in these areas in the [^{18}F] FEOBV group comparison (Figure 4C). Taken together, these findings indicate that spatial topographies of cortical degeneration in AD reflect the anatomical topography of the cholinergic projection system, and thus suggest the loss of cortical cholinergic input from the BF might play a major role in the emergence of cortico-amygdalar gray matter degeneration.

DISCUSSION

We demonstrated that the MS/DBB and NbM subregions of the basal forebrain covary with segregated topographies of cortical degeneration (Figure 3). These topographies align closely with the known anatomical segregation between the cholinergic projections of the MS/DBB and NbM subregions (Bloem et al., 2014; Hecker and Mesulam, 1994; Kondo and Zaborszky, 2016; Mesulam et al., 1983a, 1986; Zaborszky et al., 2015). We then used [^{18}F] FEOBV PET indices of binding with the vesicular acetylcholine transporter (VAChT) to demonstrate that cortical cholinergic denervation in AD exhibits spatial correspondence with our BF-dependent structural degeneration maps (Figure 4).

If the cholinergic BF neurons are selectively vulnerable to perturbed energy homeostasis, oxidative stress, and neuroinflammation due to their large axons (Lewis et al., 2010; Mattson and Magnus, 2006; Wang et al., 2010; Wu et al., 2014), they might lose the capacity to maintain full trophic support of these large axons over the course of aging. Lending support to this hypothesis, the number of cholinergic fibers per BF neuron reduces in early middle age, and especially in the transition from preclinical to MCI stages of AD, against a background of accumulating intraneuronal Aβ, hyper-phosphorylated Tau, and neurofibrillary tangles (Arendt et al., 2015; Baker-Nigh et al., 2015; Braak and Braak, 1991; Braak and Del Tredici, 2015; Geula et al., 2008; Mesulam et al., 2004; Mesulam, 2013; Schliebs and Arendt, 2006, 2011). As a result, the cortex and amygdalae might become progressively denuded of cholinergic input, with genetic AD risk factors such as the APOE ε4 allele (Poirier et al., 1995) and reduced metabolism (Rivera et al., 2005) contributing to differentiate normal age-related from AD trajectories of cholinergic loss.

Work in non-human animals indicates that cortico-amygdalar cholinergic denervation is a pivotal event in the AD pathophysiological cascade. Among mice bred to express a deficiency in VAChT (SLC18A3) capacity, the consequent reduction in cholinergic tone across the lifespan is, by itself, sufficient to induce aggregation of Aβ and hyper-phosphorylated Tau within brain areas receiving BF cholinergic projections, such as the hippocampus (Kolisnyk et al., 2016, 2017). Under this scenario, loss of cholinergic BF projections might "seed" pathophysiological changes in their cortical and amygdalar targets due to loss of cholinergic signaling. In parallel to the loss of cholinergic input, intact but diseased cholinergic projections might also transmit Tau *trans*-synaptically to cholinoreceptvie cortico-amygdalar neurons. *Trans*-synaptic spread of Tau has been reported for glutamatergic neurons in the entorhinal and hippocampal cortices (Clavaguera et al., 2009; de Calignon et al., 2012; Khan et al., 2014), however, the findings imply a general mechanism by which AD pathology can spread from diseased neurons to functionally and anatomically connected healthy neurons. In either scenario, degeneration within cortico-amygdalar targets of cholinergic BF projections should reflect the topography of the cholinergic projections themselves. We provide additional support for this hypothesis with longitudinal structural MRI.

In humans, cholinergic hypofunction correlates with the formation of Aβ plaques, tangles containing hyper-phosphorylated Tau and clinical severity of AD (Auld et al., 2002; Fisher, 2012). We observed that in addition to abnormal CSF Aβ concentration (that was used as a grouping variable), both CSF phosphorylated Tau and total Tau were significantly elevated in the AAβ MCI compared to the NAβ CN group (Table S1). Although we cannot infer from CSF data where and how these biomarkers are distributed in the brain, our findings demonstrate that in the MCI group longitudinal gray matter degeneration within the cortico-amygdalar cholinergic BF projection system, as well as cognitive decline, occurred against a biomolecular background of significant neuropathology. Nevertheless, in humans, stronger connections are needed to link the progression of cortical cholinergic denervation to its potentially very early roles in driving cortical neuropathology and altering cortical functions important for cognition, such as selective attention (Romberg et al., 2013; Schmitz et al., 2010, 2014; Schmitz and Duncan, 2018).

Standard T1-weighted sMRI measures of gray matter volume cannot distinguish different cell types. Hence, we cannot infer from our sMRI data alone whether longitudinal reductions in gray matter within the BF reflect a selective loss of cholinergic cell bodies, or some combination of cholinergic, GABAergic, and glutamatergic neurons known to co-populate its MS/DBB and NbM subregions (Henny and Jones, 2008; Lin et al., 2015). The [^{18}F] FEOBV PET radiotracer obviates this limitation. Unlike FDG and amyloid radiotracers, [^{18}F] FEOBV provides a highly sensitive and selective biomarker of central cholinergic integrity—VAChT binding (Aghourian et al., 2017). In the present study, we did not have access to longitudinal structural MRI and [^{18}F] FEOBV PET within the same individuals. Although we assessed the spatial convergence between imaging modalities using conjunction analysis in MNI template space, the accuracy of co-registration between modalities can be further improved by acquiring high-resolution PET and structural MRI within the same individuals. Finally, we note that [^{18}F] FEOBV PET was acquired in AD participants who were actively taking ACHE inhibitors to treat cognitive symptoms. Systematic investigation is required to determine whether these drugs might influence [^{18}F] FEOBV binding.

Future work will benefit from a within-subjects multimodal imaging strategy combining longitudinal [^{18}F] FEOBV PET with structural MRI, as well as direct evaluation of how pharmacological intervention with ACHE inhibitors influences these measures. Nevertheless, our present findings underscore the need for *in vivo* measures of cell-type-specific degeneration of the cholinergic system. Longitudinal monitoring of [^{18}F] FEOBV binding in cohorts of cognitively normal APOE ε4 carriers and non-carriers, in combination with CSF biomarker indices of neuropathology, will provide novel insights into the differential trajectories of the neurotypical and preclinical aging brain.

EXPERIMENTAL PROCEDURES

Structural MRI

Data used in the preparation of this article were obtained from the Alzheimer's Disease Neuroimaging Initiative (ADNI) database (http://adni.loni.usc.edu). The ADNI was launched in 2003 as a public-private partnership, led by Principal Investigator Michael W. Weiner, MD. The primary goal of ADNI has been to test whether serial magnetic resonance imaging (MRI), positron emission tomography (PET), cerebrospinal fluid (CSF) biomarkers, and clinical and neuropsychological assessment can be combined to measure the progression of mild cognitive impairment (MCI) and early Alzheimer's disease (AD).

Methodological steps for group classification (cognitively normal and early AD), structural MRI preprocessing, and definition of basal forebrain ROIs are in the Supplemental Information.

Seed-to-Searchlight Analyses

Longitudinal differences in GM were computed for the combined BF (NbM, MS/DBB) ROI and the NbM and MS/DBB sub-region ROIs, for each subject. These values were entered into multiple linear regression models (either combined BF only, or both NbM and MD/DBB) as the predictor "seeds." In both cases, additional covariates included: age, sex, education, total intracranial volume, and longitudinal change in whole brain volume. The dependent measure was the longitudinal difference in GM within a 6-mm radius spherical searchlight ROI. Over successive iterations, the searchlight was positioned at every voxel constrained within the population-average gray matter mask, producing a seed-to-searchlight map. At each searchlight the multiple linear regression was computed with the robust fitting method (i.e., robust regression) (Wilcox, 2004) to reduce potential outlier effects. Code for the seed-to-searchlight analyses was adapted from the freely available RSA Toolbox (Nili et al., 2014). Statistical significance on the searchlight maps was determined at a FDR-corrected $p < 0.05$.

^{18}[F] FEOBV PET

The [^{18}F] FEOBV PET radiotracer was acquired in 12 participants: six patients diagnosed with probable AD and six age-matched healthy volunteers (Table S4). These sample sizes are similar to those of previous rodent studies comparing FEOBV binding between an experimental group with induced mild cholinergic lesions and controls (Cyr et al., 2014; Parent et al., 2012). All participants were recruited at the McGill Centre for Studies in Aging (MCSA) and assessed at the McConnell Brain Imaging Unit (BIC) of the Montreal Neurological Institute (MNI). The original study protocol was approved by "Université du Québec à Montréal" (UQAM), and McGill University Research Ethics Boards. Informed consent was obtained from all subjects prior to participation in the study.

Methodological steps for group classification (cognitively normal and early AD) and [^{18}F] FEOBV PET preprocessing are in the Supplemental Information.

ANCOVA Model

We used SPM12 (http://www.fil.ion.ucl.ac.uk/spm/software/spm12/) to conduct a between groups analysis (CN versus AD). The parameters for the general linear model specification were as follows: threshold masking = relative (0.8), global calculation = mean voxel value, global normalization = overall grand mean scaling (50); normalization = ANCOVA. Other parameter fields were set to default values. Age was modeled as a covariate of non-interest in the model. Statistical significance on the between group contrast (CN > AD) was determined at a cluster-level FDR-corrected $p < 0.05$.

SUPPLEMENTAL INFORMATION

Supplemental Information includes Supplemental Experimental Procedures, two figures, and four tables and can be found with this article online at https://doi.org/10.1016/j.celrep.2018.06.001.

ACKNOWLEDGMENTS

Data collection and sharing for this project were funded by the Alzheimer's Disease Neuroimaging Initiative (ADNI) (NIH grant U01 AG024904) and DOD ADNI (Department of Defense award number W81XWH-12-2-0012). ADNI is funded by the National Institute on Aging, the National Institute of Biomedical Imaging and Bioengineering, and through generous contributions from the following: AbbVie, Alzheimer's Association; Alzheimer's Drug Discovery Foundation; Araclon Biotech; BioClinica; Biogen; Bristol-Myers Squibb Company; CereSpir; Eisai; Elan Pharmaceuticals; Eli Lilly and Company; EuroImmun; F. Hoffmann-La Roche Ltd and its affiliated company Genentech; Fujirebio; GE Healthcare; IXICO; Janssen Alzheimer Immunotherapy Research & Development, LLC.; Johnson & Johnson Pharmaceutical Research & Development, LLC.; Lumosity; Lundbeck; Merck & Co.; Meso Scale Diagnostics, LLC.; NeuroRx Research; Neurotrack Technologies; Novartis Pharmaceuticals Corporation; Pfizer; Piramal Imaging; Servier; Takeda Pharmaceutical Company; and Transition Therapeutics. The Canadian Institutes of Health Research is providing funds to support ADNI clinical sites in Canada. Private sector contributions are facilitated by the Foundation for the National Institutes of Health (https://fnih.org). The grantee organization is the Northern California Institute for Research and Education, and the study is coordinated by the Alzheimer's disease Cooperative Study at the University of California, San Diego. ADNI data are disseminated by the Laboratory for Neuro Imaging at the University of Southern California. This work was supported in part by a grant from the NIA (R03 RAG060263A) (T.W.S. and R.N.S.), the Canada First Research Excellence Fund (T.W.S. and R.N.S.), and the British Academy Postdoctoral Fellowship PS140117 (M.M.).

Data used in preparation of this article were obtained from the Alzheimer's Disease Neuroimaging Initiative (ADNI) database (http://adni.loni.usc.edu). As such, the investigators within the ADNI contributed to the design and implementation of ADNI and/or provided data but did not participate in analysis or writing of this report. A complete listing of ADNI investigators can be found at: http://adni.loni.usc.edu/wp-content/uploads/how_to_apply/ADNI_Acknowledgement_List.pdf.

AUTHOR CONTRIBUTIONS

ADNI collected all data, with the exception of the [^{18}F] FEOBV PET experiments, which were collected by M.A. and M.-A.B. The ADNI data were preprocessed by R.N.S. The [^{18}F] FEOBV PET data were preprocessed by M.A. and M.-A.B. All additional analyses on the ADNI and [^{18}F] FEOBV PET data were conducted by T.W.S. and M.M. T.W.S. and R.N.S. wrote the paper, with the exception of the [^{18}F] FEOBV PET methods (M.A. and M.-A.B.).

DECLARATION OF INTERESTS

The authors declare no competing interests.

Received: November 14, 2017
Revised: April 9, 2018
Accepted: May 30, 2018
Published: July 3, 2018

REFERENCES

Aghourian, M., Legault-Denis, C., Soucy, J.P., Rosa-Neto, P., Gauthier, S., Kostikov, A., Gravel, P., and Bédard, M.A. (2017). Quantification of brain cholinergic denervation in Alzheimer's disease using PET imaging with [^{18}F]-FEOBV. Mol. Psychiatry *22*, 1531–1538.

Alexander-Bloch, A., Giedd, J.N., and Bullmore, E. (2013). Imaging structural co-variance between human brain regions. Nat. Rev. Neurosci. *14*, 322–336.

Arendt, T., Brückner, M.K., Morawski, M., Jäger, C., and Gertz, H.J. (2015). Early neurone loss in Alzheimer's disease: cortical or subcortical? Acta Neuropathol. Commun. *3*, 10.

Auld, D.S., Kornecook, T.J., Bastianetto, S., and Quirion, R. (2002). Alzheimer's disease and the basal forebrain cholinergic system: relations to beta-amyloid peptides, cognition, and treatment strategies. Prog. Neurobiol. *68*, 209–245.

Baker-Nigh, A., Vahedi, S., Davis, E.G., Weintraub, S., Bigio, E.H., Klein, W.L., and Geula, C. (2015). Neuronal amyloid-β accumulation within cholinergic basal forebrain in ageing and Alzheimer's disease. Brain *138*, 1722–1737.

Ballinger, E.C., Ananth, M., Talmage, D.A., and Role, L.W. (2016). Basal forebrain cholinergic circuits and signaling in cognition and cognitive decline. Neuron *91*, 1199–1218.

Bassett, D.S., Bullmore, E., Verchinski, B.A., Mattay, V.S., Weinberger, D.R., and Meyer-Lindenberg, A. (2008). Hierarchical organization of human cortical networks in health and schizophrenia. J. Neurosci. *28*, 9239–9248.

Bloem, B., Schoppink, L., Rotaru, D.C., Faiz, A., Hendriks, P., Mansvelder, H.D., van de Berg, W.D., and Wouterlood, F.G. (2014). Topographic mapping between basal forebrain cholinergic neurons and the medial prefrontal cortex in mice. J. Neurosci. *34*, 16234–16246.

Braak, H., and Braak, E. (1991). Neuropathological stageing of Alzheimer-related changes. Acta Neuropathol. *82*, 239–259.

Braak, H., and Del Tredici, K. (2015). The preclinical phase of the pathological process underlying sporadic Alzheimer's disease. Brain *138*, 2814–2833.

Buckner, R.L., Snyder, A.Z., Shannon, B.J., LaRossa, G., Sachs, R., Fotenos, A.F., Sheline, Y.I., Klunk, W.E., Mathis, C.A., Morris, J.C., and Mintun, M.A. (2005). Molecular, structural, and functional characterization of Alzheimer's disease: evidence for a relationship between default activity, amyloid, and memory. J. Neurosci. *25*, 7709–7717.

Cantero, J.L., Zaborszky, L., and Atienza, M. (2017). Volume loss of the nucleus basalis of Meynert is associated with atrophy of innervated regions in mild cognitive impairment. Cereb. Cortex *27*, 3881–3889.

Chandler, D.J., Lamperski, C.S., and Waterhouse, B.D. (2013). Identification and distribution of projections from monoaminergic and cholinergic nuclei to functionally differentiated subregions of prefrontal cortex. Brain Res. *1522*, 38–58.

Chen, Z.J., He, Y., Rosa-Neto, P., Germann, J., and Evans, A.C. (2008). Revealing modular architecture of human brain structural networks by using cortical thickness from MRI. Cereb. Cortex *18*, 2374–2381.

Clavaguera, F., Bolmont, T., Crowther, R.A., Abramowski, D., Frank, S., Probst, A., Fraser, G., Stalder, A.K., Beibel, M., Staufenbiel, M., et al. (2009). Transmission and spreading of tauopathy in transgenic mouse brain. Nat. Cell Biol. *11*, 909–913.

Cyr, M., Parent, M.J., Mechawar, N., Rosa-Neto, P., Soucy, J.P., Aliaga, A., Kostikov, A., Maclaren, D.A., Clark, S.D., and Bedard, M.A. (2014). PET imaging with [^{18}F]fluoroethoxybenzovesamicol ([^{18}F]FEOBV) following selective lesion of cholinergic pedunculopontine tegmental neurons in rat. Nucl. Med. Biol. *41*, 96–101.

de Calignon, A., Polydoro, M., Suárez-Calvet, M., William, C., Adamowicz, D.H., Kopeikina, K.J., Pitstick, R., Sahara, N., Ashe, K.H., Carlson, G.A., et al. (2012). Propagation of tau pathology in a model of early Alzheimer's disease. Neuron *73*, 685–697.

de Castro, B.M., De Jaeger, X., Martins-Silva, C., Lima, R.D., Amaral, E., Menezes, C., Lima, P., Neves, C.M., Pires, R.G., Gould, T.W., et al. (2009). The vesicular acetylcholine transporter is required for neuromuscular development and function. Mol. Cell. Biol. *29*, 5238–5250.

Dupre, E., and Spreng, R.N. (2017). Structural covariance networks across the lifespan, from 6 to 94 years of age. Netw. Neurosci. *1*, 302–323.

Fisher, A. (2012). Cholinergic modulation of amyloid precursor protein processing with emphasis on M1 muscarinic receptor: perspectives and challenges in treatment of Alzheimer's disease. J. Neurochem. *120* (*Suppl 1*), 22–33.

Geula, C., Nagykery, N., Nicholas, A., and Wu, C.K. (2008). Cholinergic neuronal and axonal abnormalities are present early in aging and in Alzheimer disease. J. Neuropathol. Exp. Neurol. *67*, 309–318.

Grothe, M., Heinsen, H., and Teipel, S. (2013). Longitudinal measures of cholinergic forebrain atrophy in the transition from healthy aging to Alzheimer's disease. Neurobiol. Aging *34*, 1210–1220.

Grothe, M., Kilimann, I., Grinberg, L., Heinsen, H., and Teipel, S. (2018). In vivo volumetry of the cholinergic basal forebrain. Neuromethods, 213–232.

He, Y., Chen, Z.J., and Evans, A.C. (2007). Small-world anatomical networks in the human brain revealed by cortical thickness from MRI. Cereb. Cortex *17*, 2407–2419.

Hecker, S., and Mesulam, M.M. (1994). Two types of cholinergic projections to the rat amygdala. Neuroscience *60*, 383–397.

Henny, P., and Jones, B.E. (2008). Projections from basal forebrain to prefrontal cortex comprise cholinergic, GABAergic and glutamatergic inputs to pyramidal cells or interneurons. Eur. J. Neurosci. *27*, 654–670.

Khan, U.A., Liu, L., Provenzano, F.A., Berman, D.E., Profaci, C.P., Sloan, R., Mayeux, R., Duff, K.E., and Small, S.A. (2014). Molecular drivers and cortical spread of lateral entorhinal cortex dysfunction in preclinical Alzheimer's disease. Nat. Neurosci. *17*, 304–311.

Kilimann, I., Hausner, L., Fellgiebel, A., Filippi, M., Würdemann, T.J., Heinsen, H., and Teipel, S.J. (2017). Parallel atrophy of cortex and basal forebrain cholinergic system in mild cognitive impairment. Cereb. Cortex *27*, 1841–1848.

Kolisnyk, B., Al-Onaizi, M., Soreq, L., Barbash, S., Bekenstein, U., Haberman, N., Hanin, G., Kish, M.T., Souza da Silva, J., Fahnestock, M., et al. (2017). Cholinergic surveillance over hippocampal RNA metabolism and Alzheimer's-like pathology. Cereb. Cortex *27*, 3553–3567.

Kolisnyk, B., Al-Onaizi, M.A., Xu, J., Parfitt, G.M., Ostapchenko, V.G., Hanin, G., Soreq, H., Prado, M.A., and Prado, V.F. (2016). Cholinergic regulation of hnRNPA2/B1 translation by M1 muscarinic receptors. J. Neurosci. *36*, 6287–6296.

Kondo, H., and Zaborszky, L. (2016). Topographic organization of the basal forebrain projections to the perirhinal, postrhinal, and entorhinal cortex in rats. J. Comp. Neurol. *524*, 2503–2515.

Kriegeskorte, N., Goebel, R., and Bandettini, P. (2006). Information-based functional brain mapping. Proc. Natl. Acad. Sci. USA *103*, 3863–3868.

Lewis, N.E., Schramm, G., Bordbar, A., Schellenberger, J., Andersen, M.P., Cheng, J.K., Patel, N., Yee, A., Lewis, R.A., Eils, R., et al. (2010). Large-scale in silico modeling of metabolic interactions between cell types in the human brain. Nat. Biotechnol. *28*, 1279–1285.

Lin, S.C., Brown, R.E., Hussain Shuler, M.G., Petersen, C.C., and Kepecs, A. (2015). Optogenetic dissection of the basal forebrain neuromodulatory control of cortical activation, plasticity, and cognition. J. Neurosci. *35*, 13896–13903.

Mattson, M.P., and Magnus, T. (2006). Ageing and neuronal vulnerability. Nat. Rev. Neurosci. *7*, 278–294.

Mesulam, M.M. (2013). Cholinergic circuitry of the human nucleus basalis and its fate in Alzheimer's disease. J. Comp. Neurol. *521*, 4124–4144.

Mesulam, M.M., and Geula, C. (1988). Nucleus basalis (Ch4) and cortical cholinergic innervation in the human brain: observations based on the distribution of acetylcholinesterase and choline acetyltransferase. J. Comp. Neurol. *275*, 216–240.

Mesulam, M.M., Mufson, E.J., Levey, A.I., and Wainer, B.H. (1983a). Cholinergic innervation of cortex by the basal forebrain: cytochemistry and cortical connections of the septal area, diagonal band nuclei, nucleus basalis (substantia innominata), and hypothalamus in the rhesus monkey. J. Comp. Neurol. *214*, 170–197.

Mesulam, M.M., Mufson, E.J., Wainer, B.H., and Levey, A.I. (1983b). Central cholinergic pathways in the rat: an overview based on an alternative nomenclature (Ch1-Ch6). Neuroscience *10*, 1185–1201.

Mesulam, M.M., Mufson, E.J., and Wainer, B.H. (1986). Three-dimensional representation and cortical projection topography of the nucleus basalis (Ch4) in the macaque: concurrent demonstration of choline acetyltransferase and retrograde transport with a stabilized tetramethylbenzidine method for horseradish peroxidase. Brain Res. *367*, 301–308.

Mesulam, M., Shaw, P., Mash, D., and Weintraub, S. (2004). Cholinergic nucleus basalis tauopathy emerges early in the aging-MCI-AD continuum. Ann. Neurol. *55*, 815–828.

Mueller, S.G., Weiner, M.W., Thal, L.J., Petersen, R.C., Jack, C.R., Jagust, W., Trojanowski, J.Q., Toga, A.W., and Beckett, L. (2005). Ways toward an early diagnosis in Alzheimer's disease: the Alzheimer's Disease Neuroimaging Initiative (ADNI). Alzheimers Dement. *1*, 55–66.

Nichols, T., Brett, M., Andersson, J., Wager, T., and Poline, J.B. (2005). Valid conjunction inference with the minimum statistic. Neuroimage *25*, 653–660.

Nili, H., Wingfield, C., Walther, A., Su, L., Marslen-Wilson, W., and Kriegeskorte, N. (2014). A toolbox for representational similarity analysis. PLoS Comput. Biol. *10*, e1003553.

Parent, M., Bedard, M.A., Aliaga, A., Soucy, J.P., Landry St-Pierre, E., Cyr, M., Kostikov, A., Schirrmacher, E., Massarweh, G., and Rosa-Neto, P. (2012). PET imaging of cholinergic deficits in rats using [18F]fluoroethoxybenzovesamicol ([18F]FEOBV). Neuroimage *62*, 555–561.

Poirier, J., Delisle, M.C., Quirion, R., Aubert, I., Farlow, M., Lahiri, D., Hui, S., Bertrand, P., Nalbantoglu, J., Gilfix, B.M., and Gauthier, S. (1995). Apolipoprotein E4 allele as a predictor of cholinergic deficits and treatment outcome in Alzheimer disease. Proc. Natl. Acad. Sci. USA *92*, 12260–12264.

Prado, V.F., Roy, A., Kolisnyk, B., Gros, R., and Prado, M.A. (2013). Regulation of cholinergic activity by the vesicular acetylcholine transporter. Biochem. J. *450*, 265–274.

Raj, A., Kuceyeski, A., and Weiner, M. (2012). A network diffusion model of disease progression in dementia. Neuron *73*, 1204–1215.

Raj, A., LoCastro, E., Kuceyeski, A., Tosun, D., Relkin, N., and Weiner, M.; for the Alzheimer's Disease Neuroimaging Initiative (ADNI) (2015). Network diffusion model of progression predicts longitudinal patterns of atrophy and metabolism in Alzheimer's disease. Cell Rep. Published online January 14, 2015. https://doi.org/10.1016/j.celrep.2014.12.034.

Rivera, E.J., Goldin, A., Fulmer, N., Tavares, R., Wands, J.R., and de la Monte, S.M. (2005). Insulin and insulin-like growth factor expression and function deteriorate with progression of Alzheimer's disease: link to brain reductions in acetylcholine. J. Alzheimers Dis. *8*, 247–268.

Romberg, C., Bussey, T.J., and Saksida, L.M. (2013). Paying more attention to attention: towards more comprehensive cognitive translation using mouse models of Alzheimer's disease. Brain Res. Bull. *92*, 49–55.

Schliebs, R., and Arendt, T. (2006). The significance of the cholinergic system in the brain during aging and in Alzheimer's disease. J. Neural Transm. (Vienna) *113*, 1625–1644.

Schliebs, R., and Arendt, T. (2011). The cholinergic system in aging and neuronal degeneration. Behav. Brain Res. *221*, 555–563.

Schmitz, T.W., and Duncan, J. (2018). Normalization and the cholinergic microcircuit: a unified basis for attention. Trends Cogn. Sci. *22*, 422–437.

Schmitz, T.W., Cheng, F.H., and De Rosa, E. (2010). Failing to ignore: paradoxical neural effects of perceptual load on early attentional selection in normal aging. J. Neurosci. *30*, 14750–14758.

Schmitz, T.W., Dixon, M.L., Anderson, A.K., and De Rosa, E. (2014). Distinguishing attentional gain and tuning in young and older adults. Neurobiol. Aging *35*, 2514–2525.

Schmitz, T.W., and Spreng, R.N.; Alzheimer's Disease Neuroimaging Initiative (2016). Basal forebrain degeneration precedes and predicts the cortical spread of Alzheimer's pathology. Nat. Commun. *7*, 13249.

Seeley, W.W., Crawford, R.K., Zhou, J., Miller, B.L., and Greicius, M.D. (2009). Neurodegenerative diseases target large-scale human brain networks. Neuron *62*, 42–52.

Shaw, L.M., Vanderstichele, H., Knapik-Czajka, M., Clark, C.M., Aisen, P.S., Petersen, R.C., Blennow, K., Soares, H., Simon, A., Lewczuk, P., et al.; Alzheimer's Disease Neuroimaging Initiative (2009). Cerebrospinal fluid biomarker signature in Alzheimer's disease neuroimaging initiative subjects. Ann. Neurol. *65*, 403–413.

Spreng, R.N., and Turner, G.R. (2013). Structural covariance of the default network in healthy and pathological aging. J. Neurosci. *33*, 15226–15234.

Wang, X., Michaelis, M.L., and Michaelis, E.K. (2010). Functional genomics of brain aging and Alzheimer's disease: focus on selective neuronal vulnerability. Curr. Genomics *11*, 618–633.

Wilcox, R. (2004). Introduction to Robust Estimation and Hypothesis Testing, Second Edition (Academic Press).

Woo, C.W., Krishnan, A., and Wager, T.D. (2014). Cluster-extent based thresholding in fMRI analyses: pitfalls and recommendations. Neuroimage *91*, 412–419.

Wu, H., Williams, J., and Nathans, J. (2014). Complete morphologies of basal forebrain cholinergic neurons in the mouse. eLife *3*, e02444.

Zaborszky, L., Hoemke, L., Mohlberg, H., Schleicher, A., Amunts, K., and Zilles, K. (2008). Stereotaxic probabilistic maps of the magnocellular cell groups in human basal forebrain. Neuroimage *42*, 1127–1141.

Zaborszky, L., Csordas, A., Mosca, K., Kim, J., Gielow, M.R., Vadasz, C., and Nadasdy, Z. (2015). Neurons in the basal forebrain project to the cortex in a complex topographic organization that reflects corticocortical connectivity patterns: an experimental study based on retrograde tracing and 3D reconstruction. Cereb. Cortex *25*, 118–137.

Cell Reports, Volume *24*

Supplemental Information

Longitudinal Alzheimer's Degeneration Reflects the Spatial Topography of Cholinergic Basal Forebrain Projections

Taylor W. Schmitz, Marieke Mur, Meghmik Aghourian, Marc-Andre Bedard, R. Nathan Spreng, and for the Alzheimer's Disease Neuroimaging Initiative

Supplemental Data Items

Figure S1 title: Coregistration of BF ROIs with an example MCI individual. Related to Experimental Procedures.

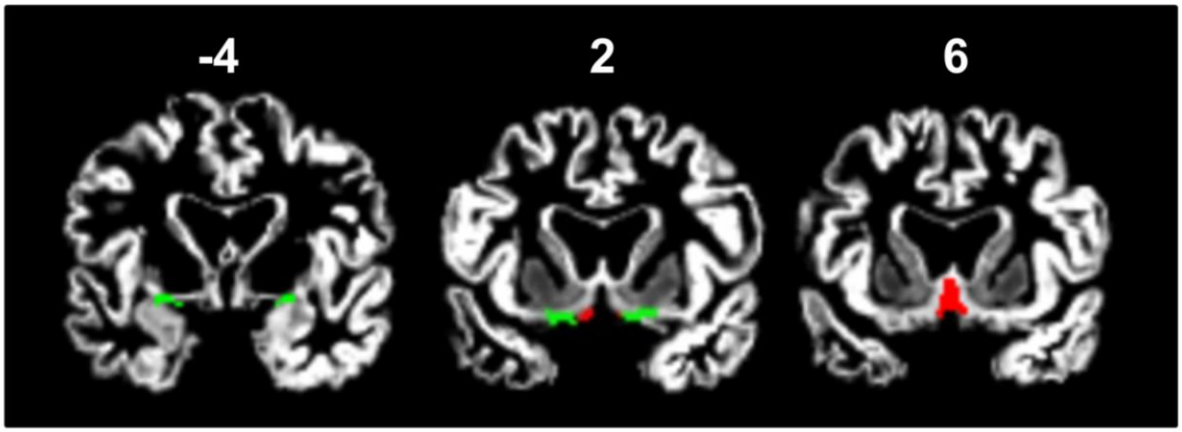

Figure S1 caption: The basal forebrain regions of interest (ROIs) are displayed on the modulated GM volume of a representative MCI AAβ participant. The green overlay corresponds to the nucleus basalis of Meynert (NbM). The red overlay corresponds to the medial septal nucleus/diagonal band of Broca (MS/DBB). Slices are in coronal plane with MNI coordinates (*y*-axis).

Figure S2 title: Standardized uptake values for the [^{18}F] FEOBV PET radiotracer. Related to Results and Experimental Procedures.

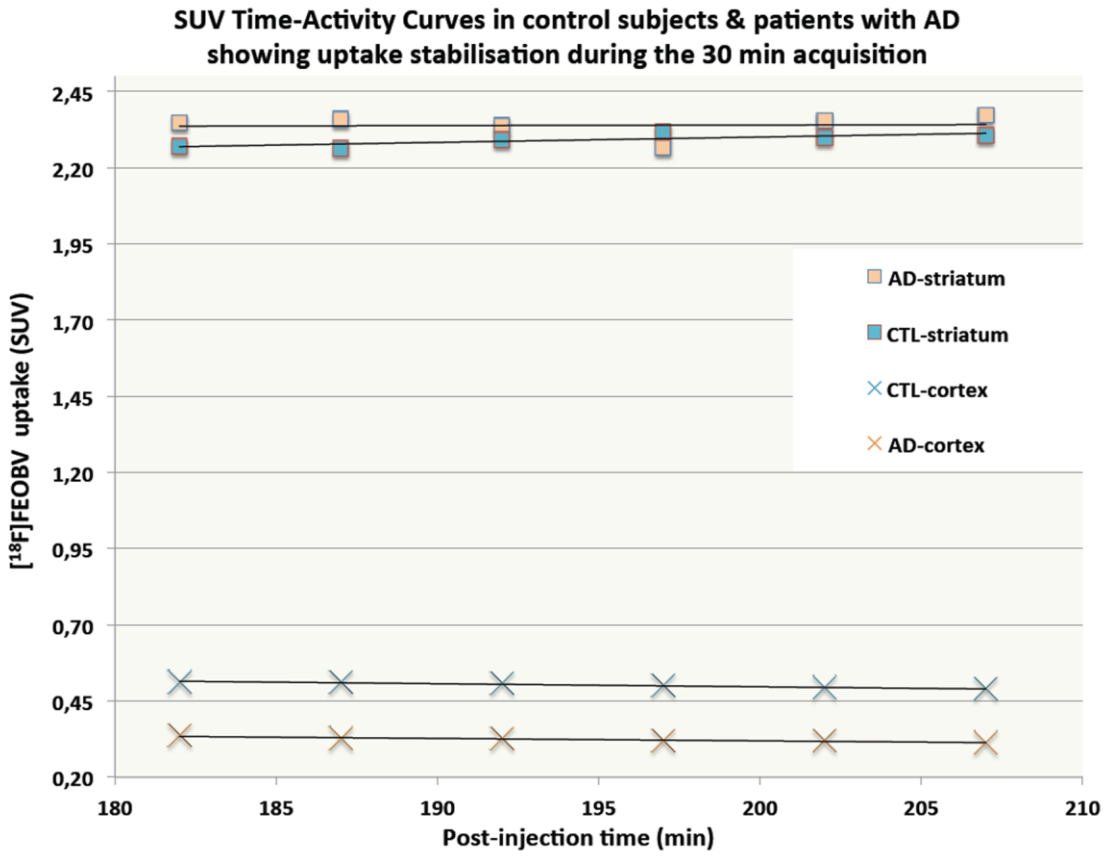

Figure S2 caption: Standardized uptake values (SUVs) are shown for the [^{18}F] FEOBV PET radiotracer (*y*-axis) during the 30 minute experimental acquisition window (*x*-axis), which occurred 3 hours after injection.

Table S1: Characteristics of the ADNI CN NAβ and MCI AAβ groups. Related to Results and Experimental Procedures.

	Subgroups		
Demographics	**$CN_{NA\beta}$**	**$MCI_{AA\beta}$**	***t*-test**
Sex (Male, Female)	52 (25, 27)	80 (53, 27)	t=2.01, p=0.04
Age (years ± SD)	75.1 ± 4.5	73.9 ± 6.9	t=1.27, p=0.21
Education (years ± SD)	15.7 ± 2.8	15.9 ± 3.1	t=0.42, p=0.68
Scan interval (days ± SD)	762.8 ± 26.6	743.7 ± 101.7	t=1.60, p=0.11
CSF measure			
$A\beta_{1\text{-}42}$ (pg/Ml ± SD)	242.5 ± 26.6	136.5 ± 25.3	t=22.8, p<0.001
Total Tau (pg/Ml ± SD)	63.8 ± 22.03	106.3 ± 51.9	t=6.45, p<0.001
p-Tau_{181p} (pg/Ml ± SD)	21.3 ± 8.15	39.2 ± 17.4	t=7.97, p<0.001
Cognitive measure			
1 Logical Mem. Imm. (± SD)	13.75 ± 3.02	6.76 ± 3.09	t=12.44, p<0.001
2 Logical Mem. Imm. (± SD)	15.31 ± 3.41	5.55 ± 3.80	t=14.84, p<0.001
1 – 2 Logical Mem. Imm. (± SD)	-1.56 ± 2.86***	0.71 ± 3.84*	t=3.65, p<0.001
1 Logical Mem. Del. (± SD)	12.85 ± 3.50	3.06 ± 2.57	t=17.79, p<0.001
2 Logical Mem. Del. (± SD)	13.9 ± 4.17	2.77 ± 3.63	t=15.95, p<0.001
1 – 2 Logical Mem. Del. (± SD)	-1.06 ± 3.99	0.08 ± 2.59	t=1.98, p=0.05
1 RAVLT Imm. (± SD)	8.02 ± 3.17	3.14 ± 2.85	t=9.18, p<0.001
2 RAVLT Imm. (± SD)	8.69 ± 2.69	2.38 ± 2.60	t=13.45, p<0.001
1 – 2 RAVLT Imm. (± SD)	-0.67 ± 3.33	0.76 ± 3.14*	t=2.51, p=0.01
1 RAVLT Del. (± SD)	7.37 ± 3.82	1.98 ± 2.80	t=9.34, p<0.001
2 RAVLT Del. (± SD)	8.17 ± 3.43	1.36 ± 2.41	t=13.36, p<0.001
1 – 2 RAVLT Del. (± SD)	-0.81 ± 3.85	0.61 ± 2.17*	t=2.71, p=0.01
1 RAVLT Rec. (± SD)	13.08 ± 2.48	8.85 ± 3.75	t=7.16, p<0.001
2 RAVLT Rec. (± SD)	13.31 ± 2.07	7.8 ± 4.21	t=8.74, p<0.001
1 – 2 RAVLT Rec. (± SD)	-0.23 ± 2.91	1.05 ± 4.23*	t=1.91, *p=0.06*
1 Bost. Naming (± SD)	27.31 ± 4.55	25.48 ± 4.75	t=2.2, p=0.03
2 Bost. Naming (± SD)	28.23 ± 2.54	23.98 ± 6.17	t=4.71, p<0.001
1 – 2 Bost. Naming (± SD)	-0.92 ± 4.39	1.5 ± 3.58***	t=3.47, p<0.001
1 Sem. Flue. A (± SD)	19.29 ± 5.90	15.03 ± 4.82	t=4.54, p<0.001
2 Sem. Flue. A (± SD)	20.15 ± 5.18	13.01 ± 5.03	t=7.87, p<0.001
1 – 2 Sem. Flue. A (± SD)	-0.87 ± 5.04	2.01 ± 4.45***	t=3.45, p<0.001
1 Sem. Flue. V (± SD)	14.87 ± 3.73	9.84 ± 3.37	t=8.02, p<0.001
2 Sem. Flue. V (± SD)	15.19 ± 3.45	8.54 ± 3.90	t=10, p<0.001
1 – 2 Sem. Flue. V (± SD)	-0.33 ± 3.13	1.3 ± 3.83**	t=2.56, p=0.01
1 MMSE (± SD)	29.12 ± 1.04	26.63 ± 1.87	t=8.75, p<0.001
2 MMSE (± SD)	29.37 ± 0.88	24.04 ± 4.82	t=7.87, p<0.001

1 – 2 MMSE (± SD)	-0.25 ± 1.2	2.59 ± 4.4***	t=4.54, p<0.001
1 CDR (± SD)	0 ± 0	0.5 ± 0	t=N/A, p=N/A
2 CDR (± SD)	0.03 ± 0.11	0.71 ± 0.39	t=12, p<0.001
1 – 2 CDR (± SD)	-0.03 ± 0.12	-0.21 ± 0.4***	t=3.14, p=0.002

Table S1 caption: Tabled values are the mean ± standard deviation for groups drawn from the Alzheimer's Disease Neuroimaging Initiative (ADNI) database. All *t*-statistics reported in the right-most column are independent samples *t*-tests between the cognitively normal adults with normal cerebrospinal fluid biomarker status ($CN_{NA\beta}$) and the adults with mild cognitive impairment adults and abnormal cerebrospinal fluid biomarker states ($MCI_{AA\beta}$). CSF measures: $A\beta_{1\text{-}42}$ = amyloid Beta 1 to 42 peptide, p-Tau_{181p} = Tau phosphorylated at threonine181, pg/Ml = picograms/millilitres (concentration solution). Neuropsychological test abbreviations: Logical Mem. = Logical Memory (Imm. = Immediate, Del. = Delayed); RAVLT = Rey Auditory Verbal Learning Test (Imm. = Immediate, Del. = Delayed, Rec. = Recall); Bost. Naming = Boston Naming Test; Sem. Flu. = Semantic Fluency (A = Auditory, V = Visual); MMSE = Mini-mental State Exam; CDR = Clinical Dementia Rating. For all neuropsychological measures, total scores are reported separately for the two visits (Time 1 and Time 2) and for the difference between visits (Time 1 – Time 2). Significant within groups differences between Time 1 and Time 2 are denoted by asterisks (***p<0.001, **p<0.005, *p<0.05). N/A = not applicable due to zero standard deviation in both groups (100% classification). Cognitive differences are assessed using a 2-tailed alpha.

Table S2: ADNI participant information for included subjects. Related to Experimental Procedures.

Research ID	Diagnostic Group	Image ID Time 1	Image ID Time 2	Aβcut
14	CN	59375	87012	NAβ
23	CN	32409	200416	NAβ
31	CN	118843	86359	NAβ
40	CN	34607	87622	NAβ
61	CN	119062	87055	NAβ
66	CN	59446	85934	NAβ
89	CN	49675	94601	NAβ
96	CN	59456	96248	NAβ
118	CN	34114	96275	NAβ
120	CN	34332	98785	NAβ
123	CN	63784	106567	NAβ
127	CN	130234	101739	NAβ
159	CN	33489	97039	NAβ
172	CN	65757	102790	NAβ
177	CN	34806	133406	NAβ
260	CN	34384	106551	NAβ
327	CN	79732	108286	NAβ
352	CN	34537	104476	NAβ
386	CN	49680	123913	NAβ
413	CN	45117	120917	NAβ
441	CN	48029	107925	NAβ
454	CN	79755	108571	NAβ
459	CN	46629	105949	NAβ
472	CN	118702	129183	NAβ
488	CN	107934	109943	NAβ
498	CN	55943	124026	NAβ
516	CN	42308	109925	NAβ
519	CN	39647	123626	NAβ
533	CN	38785	112310	NAβ
559	CN	40674	120949	NAβ
602	CN	32672	122635	NAβ
605	CN	38861	123328	NAβ
610	CN	32667	122640	NAβ
618	CN	67110	123017	NAβ
637	CN	118711	122791	NAβ
648	CN	59666	123289	NAβ
657	CN	59739	123303	NAβ
677	CN	119102	123872	NAβ
680	CN	38926	123337	NAβ
685	CN	40683	120994	NAβ
686	CN	46668	123971	NAβ
866	CN	65611	125011	NAβ
886	CN	39171	124165	NAβ
896	CN	56031	128551	NAβ
923	CN	42509	162091	NAβ
926	CN	31547	125020	NAβ
1002	CN	65220	139311	NAβ
1016	CN	42772	133901	NAβ
1169	CN	119118	141216	NAβ

1190	CN	46417	138005	NAβ
1206	CN	59981	140777	NAβ
1250	CN	62240	143901	NAβ
41	MCI-P	118697	129868	AAβ
57	MCI-P	119796	91468	AAβ
77	MCI-P	68120	133465	AAβ
101	MCI-P	63297	134657	AAβ
204	MCI-P	39542	99196	AAβ
222	MCI-P	54686	102450	AAβ
256	MCI-P	34150	79568	AAβ
269	MCI-P	65257	80424	AAβ
336	MCI-P	34857	133423	AAβ
344	MCI-P	36579	108040	AAβ
388	MCI-P	81396	166912	AAβ
394	MCI-P	34398	123776	AAβ
507	MCI-P	80199	112547	AAβ
567	MCI-P	42370	86686	AAβ
604	MCI-P	79191	162265	AAβ
625	MCI-P	31495	90880	AAβ
638	MCI-P	67531	129842	AAβ
649	MCI-P	74411	172339	AAβ
658	MCI-P	39701	122843	AAβ
723	MCI-P	42384	96119	AAβ
725	MCI-P	86166	121386	AAβ
729	MCI-P	40708	123994	AAβ
750	MCI-P	59561	122945	AAβ
834	MCI-P	59798	124794	AAβ
835	MCI-P	78885	162368	AAβ
839	MCI-P	80230	166957	AAβ
861	MCI-P	67918	162131	AAβ
878	MCI-P	90889	163059	AAβ
906	MCI-P	66569	162498	AAβ
941	MCI-P	34747	125038	AAβ
997	MCI-P	66630	176861	AAβ
1010	MCI-P	90566	166921	AAβ
1033	MCI-P	118718	92291	AAβ
1054	MCI-P	62234	132415	AAβ
1126	MCI-P	128366	138025	AAβ
1130	MCI-P	73037	205570	AAβ
1213	MCI-P	47223	135240	AAβ
1217	MCI-P	62984	137001	AAβ
1247	MCI-P	48857	143169	AAβ
1292	MCI-P	118746	103296	AAβ
1394	MCI-P	68082	171362	AAβ
33	MCI-NP	45166	87588	AAβ
51	MCI-NP	35819	88309	AAβ
102	MCI-NP	39460	92012	AAβ
150	MCI-NP	65130	97106	AAβ
285	MCI-NP	39117	123380	AAβ
291	MCI-NP	34524	101787	AAβ
307	MCI-NP	34159	103672	AAβ
361	MCI-NP	59753	105474	AAβ
378	MCI-NP	95688	112328	AAβ
424	MCI-NP	33644	106451	AAβ

481	MCI-NP	46647	109968	AAβ
544	MCI-NP	64672	106458	AAβ
552	MCI-NP	79796	112246	AAβ
588	MCI-NP	79824	142027	AAβ
607	MCI-NP	35938	133494	AAβ
621	MCI-NP	64189	112262	AAβ
626	MCI-NP	34672	123847	AAβ
644	MCI-NP	34240	122954	AAβ
671	MCI-NP	64161	123895	AAβ
673	MCI-NP	36949	123101	AAβ
748	MCI-NP	36959	123110	AAβ
783	MCI-NP	39152	123407	AAβ
800	MCI-NP	43035	123506	AAβ
921	MCI-NP	49510	124778	AAβ
925	MCI-NP	67266	129646	AAβ
932	MCI-NP	118715	130054	AAβ
950	MCI-NP	97200	147503	AAβ
961	MCI-NP	59601	129241	AAβ
994	MCI-NP	45943	130128	AAβ
1034	MCI-NP	47953	129585	AAβ
1046	MCI-NP	46396	139042	AAβ
1097	MCI-NP	59610	132261	AAβ
1183	MCI-NP	66167	160885	AAβ
1227	MCI-NP	63838	147855	AAβ
1268	MCI-NP	64037	143103	AAβ
1269	MCI-NP	68545	160680	AAβ
1309	MCI-NP	51605	139278	AAβ
1351	MCI-NP	59615	143667	AAβ
1419	MCI-NP	73656	162969	AAβ

Table S2 caption: CN = cognitively normal, MCI-P = Mild cognitive impairment exhibiting progression to AD in the 2 year study interval, MCI-NP = Mild cognitive impairment remaining neuropsychologically stable in the 2 year study interval. NAβ = normal cerebrospinal amyloid-β_{1-42} concentrations, AAβ = abnormal cerebrospinal amyloid-β_{1-42} concentrations.

Table S3: ADNI participant information for excluded subjects. Related to Experimental Procedures.

Research ID	Diagnostic Group	Aβcut
42	MCI-P	NAβ
107	MCI-NP	NAβ
158	MCI-NP	NAβ
214	MCI-P	N/A
240	MCI-P	NAβ
273	MCI-NP	NAβ
292	MCI-NP	NAβ
376	MCI-NP	NAβ
429	MCI-P	NAβ
448	MCI-NP	NAβ
464	MCI-NP	NAβ
579	MCI-NP	NAβ
634	MCI-NP	NAβ
746	MCI-NP	NAβ
908	MCI-NP	NAβ
912	MCI-NP	NAβ
1045	MCI-NP	NAβ
1140	MCI-NP	NAβ
1187	MCI-NP	NAβ
1260	MCI-NP	NAβ
1321	MCI-NP	NAβ
1352	MCI-NP	NAβ
1398	MCI-P	NAβ
1414	MCI-NP	NAβ

Table S3 caption: CN = cognitively normal, MCI-P = Mild cognitive impairment exhibiting progression to AD in the 2 year study interval, MCI-NP = Mild cognitive impairment remaining neuropsychologically stable in the 2 year study interval. NAβ = normal cerebrospinal amyloid-β_{1-42} concentrations, AAβ = abnormal cerebrospinal amyloid-β_{1-42} concentrations. N/A = not applicable due to missing data

Table S4: Characteristics of the [18F] FEOBV PET CN and AD groups. Related to Results and Experimental Procedures.

	Subgroups		
Demographics	**CN**	**AD**	***t*-test**
Sex (Male, Female)	6 (3, 3)	6 (3, 3)	N/A
Age (years ± SD)	67.0 ± 11.12	67.2 ± 10.24	$t<1$
Education (years ± SD)	14.7 ± 3.88	16.8 ± 5.03	$t<1$
PET			
^{18}F-NAV4694 SUVR	1.97 ± 0.87	2.82 ± 0.21	$t=2.33$, $p=0.04$
Cognitive measure			
MMSE	29.2 ± 0.41	18.3 ± 7.31	$t=3.39$, $p=0.007$
MoCA	27.0 ± 1.55	12.8 ± 6.49	$t=5.20$, $p=0.005$
GDS	1.0 ± 0.89	2.5 ± 2.16	$t=1$

Table S4 caption: Tabled values are the mean of each subgroup ± standard deviation. All *t*-statistics reported in the right-most column are independent samples *t*-tests between the cognitively normal adults (CN) and adults with Alzheimer's disease dementia (AD). PET = Positron Emission Tomography, ^{18}F-NAV4694 = Aβ radiotracer, SUVR = Standardized Uptake Value Ratio for the whole cortex. Neuropsychological test abbreviations: MMSE = Mini-Mental State Examination, MoCA= Montreal, Cognitive Assessment, GDS= Geriatric Depression Scale.

Supplemental Experimental Procedures

Structural MRI

Group classification. Staging of AD disease progression was accomplished by a two-step procedure. In the first step, individuals were partitioned according to CSF concentrations of Aβ. Individuals falling below a concentration 192 pg ml^{-1} were grouped as probable AD, in accordance with the cut-point established by both Shaw et al. (2009), and independently validated by Hansson et al (2018). In the second step, cognitive function was cross-referenced for individuals falling below and above the CSF Aβ cutpoint. Individuals with a neuropsychological evaluation of MCI and abnormal CSF Aβ were included in our MCI group (see Tables S1 and S2). Individuals with age-adjusted cognitively normal neuropsychological evaluation and normal CSF Aβ were included in our CN group (see Tables S1 and S2). This strategy allows for precise demarcation of our study cohorts (Schmitz and Spreng, 2016): CN healthy older adults are not confounded with cognitively normal adults in preclinical stages of AD; moreover, MCI adults with AD are not confounded with MCI adults with non-AD etiology, such as vascular dementia or hippocampal sclerosis (see Table S3).

Preprocessing. All subjects were required to have had two T1-weighted MRI scans acquired with the same scanner and pulse sequence. Data were preprocessed using SPM8 software (Wellcome Trust Centre for Neuroimaging, Institute of Neurology, UCL, London, UK, http://www.fil.ion.ucl.ac.uk/spm) and VBM8 toolbox (http://dbm.neuro.uni-jena.de/vbm8/) with Matlab (version 7.9.0 R2009b, The Mathworks, MA). The two scans for each participant were intra-individual realigned and averaged to reduce bias introduced by using one of the two time-point images as the reference image for computing warping parameters (Reuter and Fischl, 2011; Reuter et al., 2012). We then further pre-processed these three images using VBM8. Each image was bias-corrected and segmented into gray matter, white matter, and cerebrospinal fluid (CSF). Segmented images were quality checked for sample homogeneity using the VBM8 toolbox. For both MCI and CN adults, the within-subject average images were mapped to an iteratively evolving study-specific population mean of the gray and white matter tissues which were estimated using DARTEL (diffeomorphic anatomical registration through an exponentiated lie algebra), which minimizes the geodesic distance from each subject to the population mean (Ashburner, 2007). An affine mapping between the population mean and MNI space was also estimated and combined with each subject-to-population-mean mapping for warping the individual time-point images to MNI space. We used the normalized modulated gray matter images for subsequent region of interest and regression analyses. The increased accuracy of the DARTEL registration algorithm allows for smaller smoothing kernels in order to correct for intra- and inter-subject misalignment. Based on prior work examining simulated atrophy and DARTEL at varying smoothing kernels (Shen and Sterr, 2013), we chose a very light smoothing kernel of 4 mm^3 full width, half maximum.

Regions of interest. The SPM Anatomy Toolbox (Eickhoff et al., 2005) was used to define probabilistic anatomical maps of the BF ROI used in the initial seed-to-searchlight analysis (Figure 2), as well as the separate NbM and MS/DBB ROIs (Figure 3) used in sub-regional seed-to-searchlight analyses (Zaborszky et al., 2008). See Figure 1a and Figure S1. All ROIs included both left and right hemispheres. The ROIs were linearly coregistered with MNI space. To produce indices of longitudinal degeneration, for each participant we subtracted their unsmoothed modulated GM images at Time 2 from Time 1. Within each BF subregion, values for mean gray matter volume and longitudinal degeneration were extracted using the Marsbar toolbox (Brett et al., 2002).

[^{18}F] FEOBV PET

Group classification: As in the sMRI cohort, patients in the FEOBV cohort were confirmed as having AD according to both neuropsychological status and an independent biomarker of Aβ pathology. See Table S4. A neuropsychological status of AD was determined from the standard criteria of the 'Alzheimer's Association Workgroup on Diagnostic Guidelines for Alzheimer's Disease' (Dubois et al., 2007). In order to be included in this study, all participants were assessed with the Mini-Mental State Examination (MMSE), and the Montreal Cognitive Assessment (MoCA). The main inclusion criteria for AD patients were MMSE and MoCa scores of 26 or lower. In control subjects, only participants with MMSE and MoCA scores higher than 26 were included. Abnormal levels of brain amyloid-beta (Aβ) plaques were confirmed in patients with a neuropsychological status of AD by using PET imaging with the [^{18}F]-NAV4694 (NAV) Aβ radiotracer, with a SUVR cut off value of 1.5 or greater (Rowe et al., 2013). At the time of their enrolment, all AD patients had undergone treatment with a cholinesterase inhibitor for at least two months. Exclusion criteria were as follows: To rule out the presence of mood disorders, participants presenting with a Geriatric Depression Scale (GDS) score of over 5 were excluded; participants with other active medical or psychiatric issues that could affect cognitive function were also excluded from the study. To rule out non-AD type dementia, participants with any clinical or brain imaging evidence of vascular disease, Lewy body

disease, any form of Primary Progressive Aphasia, or frontotemporal dementia/frontal temporal lobar were excluded.

Pre-processing: On the first of two visits, participants underwent a structural T1-weighted MRI scan (1.5T Siemens Sonata), followed by a PET scan with either the [^{18}F] FEOBV or NAV tracer (Siemens HRRT), counterbalanced across participants. Within a two-week interval, participants returned for a second visit, during which a second PET scan was acquired using the remaining tracer. [^{18}F] FEOBV and NAV were synthesized at the BIC Cyclotron Facility. The precursors for both [^{18}F] FEOBV and NAV were purchased from commercial vendors (ABX Advanced Biochemical Compounds, Radeberg, Germany and NAVIDEA Biopharmaceutical, Dublin, OH, USA). Radiolabelling methods for the compounds are similar and have been described elsewhere (Mzengeza et al., 2007). Each radiotracer was administered by slow IV bolus injection with radioactive doses varying between 160 and 340 MBq. Before data acquisition, the PET scanner was calibrated by performing a standard quality control protocol. A 5 min transmission scan for attenuation correction, using a source of [137Cs], was performed before injection of the tracer. PET data acquisition was done in 3D list mode. For [^{18}F] FEOBV, static data acquisition started three hours following injection, and lasted for a 30 minutes duration, fragmented into six frames of 5 minutes, as described by Petrou et al. (2014). This allowed standard uptake values (SUV) to stabilise throughout the data acquisition (Figure S2). For NAV, data acquisition started 30 minutes following injection, and was conducted for 30 minutes over six frames of 5 minutes (Aghourian et al., 2017). A head holder was used to minimize head motion during the scan.

PET images were reconstructed using an OP-OSEM (Ordinary Poisson-Ordered Subset Expectation Maximization) algorithm correcting for scattering, random coincidences, attenuation, decay and dead time; frame-based motion correction was also performed if needed. The MINC software toolbox (http://www.bic.mni.mcgill.ca/ServicesSoftware/MINC) was used to perform five initial pre-processing steps: (1) MR images of all participants were first co-registered to the MNI-152 standard reference template by the CIVET image-processing pipeline, using a 6-parameter affine transformation and non-linear spatial normalization; (2) time-averaged PET images were normalized as a function of the injected dose of tracer and the subject's weight to obtain standard uptake values (SUVs); (3) The PET SUVs image was then co-registered to the subject's own MRI, and from there to the MNI-152 template using the linear and non-linear transformations obtained in the first step; (4) Standardized uptake value ratio (SUVR) maps were generated for [^{18}F] FEOBV and NAV by using the global cerebral white matter as the reference region due to the absence of cholinergic projections (as opposed to the cerebellar cortex which receives cholinergic projections from various brainstem nuclei).; (5) Finally, smoothing of the PET images was performed using a Gaussian kernel of 8 mm. No correction for partial volume effects was applied to the PET imaging data.

Supplemental References

Aghourian, M., Legault-Denis, C., Soucy, J.P., Rosa-Neto, P., Gauthier, S., Kostikov, A., Gravel, P., and Bedard, M.A. (2017). Quantification of brain cholinergic denervation in Alzheimer's disease using PET imaging with [18F]-FEOBV. Mol Psychiatry 11, 1531-1538.

Ashburner, J. (2007). A fast diffeomorphic image registration algorithm. Neuroimage 38, 95-113.

Brett, M., Anton, J.L., Valabregue, R., and Poline, J.B. (2002). Region of interest analysis using an SPM toolbox. In 8th International Conference on Functional Mapping of the Human Brain (Sendai, Japan, NeuroImage).

Dubois, B., Feldman, H.H., Jacova, C., Dekosky, S.T., Barberger-Gateau, P., Cummings, J., Delacourte, A., Galasko, D., Gauthier, S., Jicha, G., *et al.* (2007). Research criteria for the diagnosis of Alzheimer's disease: revising the NINCDS-ADRDA criteria. Lancet Neurol 6, 734-746.

Eickhoff, S.B., Stephan, K.E., Mohlberg, H., Grefkes, C., Fink, G.R., Amunts, K., and Zilles, K. (2005). A new SPM toolbox for combining probabilistic cytoarchitectonic maps and functional imaging data. Neuroimage 25, 1325-1335.

Hansson, O., Seibyl, J., Stomrud, E., Zetterberg, H., Trojanowski, J.Q., Bittner, T., Lifke, V., Corradini, V., Eichenlaub, U., Batrla, R., *et al.* (2018). CSF biomarkers of Alzheimer's disease concord with amyloid-beta PET and predict clinical progression: A study of fully automated immunoassays in BioFINDER and ADNI cohorts. Alzheimers Dement.

Mzengeza, S., Massarweh, G., Rosa Neto, P., Soucy, J.P., and Bedard, M.A. (2007). Radiosynthesis of [18F] FEOV and in vivo PET imaging of acetylcholine vesicular transporter in the rat. J Cereb Blood Flow Metab 27, 10-17U.

Petrou, M., Frey, K.A., Kilbourn, M.R., Scott, P.J., Raffel, D.M., Bohnen, N.I., Muller, M.L., Albin, R.L., and Koeppe, R.A. (2014). In vivo imaging of human cholinergic nerve terminals with (-)-5-(18)F-fluoroethoxybenzovesamicol: biodistribution, dosimetry, and tracer kinetic analyses. J Nucl Med 55, 396-404.

Reuter, M., and Fischl, B. (2011). Avoiding asymmetry-induced bias in longitudinal image processing. Neuroimage 57, 19-21.

Reuter, M., Schmansky, N.J., Rosas, H.D., and Fischl, B. (2012). Within-subject template estimation for unbiased longitudinal image analysis. Neuroimage 61, 1402-1418.

Rowe, C.C., Pejoska, S., Mulligan, R.S., Jones, G., Chan, J.G., Svensson, S., Cselenyi, Z., Masters, C.L., and Villemagne, V.L. (2013). Head-to-head comparison of 11C-PiB and 18F-AZD4694 (NAV4694) for beta-amyloid imaging in aging and dementia. J Nucl Med 54, 880-886.

Schmitz, T.W., and Spreng, R.N. (2016). Basal forebrain degeneration precedes and predicts the cortical spread of Alzheimer's pathology. Nat Commun 7, 13249.

Shaw, L.M., Vanderstichele, H., Knapik-Czajka, M., Clark, C.M., Aisen, P.S., Petersen, R.C., Blennow, K., Soares, H., Simon, A., Lewczuk, P., *et al.* (2009). Cerebrospinal fluid biomarker signature in Alzheimer's disease neuroimaging initiative subjects. Ann Neurol 65, 403-413.

Shen, S., and Sterr, A. (2013). Is DARTEL-based voxel-based morphometry affected by width of smoothing kernel and group size? A study using simulated atrophy. Journal of magnetic resonance imaging : JMRI 37, 1468-1475.

Zaborszky, L., Hoemke, L., Mohlberg, H., Schleicher, A., Amunts, K., and Zilles, K. (2008). Stereotaxic probabilistic maps of the magnocellular cell groups in human basal forebrain. Neuroimage 42, 1127-1141.